Personalization of a Biophysically Realistic Computational Model of the Brain Activity Using EEG and MRI Data

Roser Sanchez Todo

Universitat Pompeu Fabra
Barcelona

Personalization of a biophysically realistic computational model of the brain activity using EEG and MRI data

The first step towards a new generation of virtual experiments on personalized human brain models.

Roser Sanchez Todo

u*p*f. **Universitat Pompeu Fabra** *Barcelona*   NE neuroelectrics®

*To Josep Maria, a brilliant teacher that
made me love learning and science.*

Acknowledgments

This is not a work of one person alone, it is an output of a beautiful collaboration of enthusiastic and lovely people. I hope someday I can really thank them all for each of the small contributions to the project. Without them, I could not have achieved this far, I would not have learned that much, and I wouldn't have enjoyed doing this work as much as I did.

First, I want to thank the cornerstone of this work, Giulio, for giving me the opportunity to make it happen. I couldn't have been given a better challenge like this one. Giulio has been a guide, a teacher and a big motivation. No words can express the gratefulness I feel towards him, for this opportunity and this exciting experience. Thank you, Giulio.
Same to Ricardo, for all his enormous help and all the knowledge shared with me. Thanks for all the effort, patience, and the opportunity to work in your team, Ricardo.

Special thanks to Carla and Manuel, for their positivism and hard work. You have been always there, willing to help, and it is very much appreciated. We are a great team, together with Maria Chiara and Ricardo, and I feel lucky to have worked with all of you, thanks.

Thanks to Jordi Solis, Marta Castellano and Pawel Skorupinski. These three people can't be more passionate about their work. You have given to me a big support (in any sense) and motivation. Specially to Jordi, who has always been there willing to help. His support is really appreciated. Thanks, Jordi, I'm really lucky to have you in the team.

I want to thank Giulio again for giving me the opportunity to meet in Rennes an incredible amount of talented, enthusiastic and welcoming people from whom in two weeks I learned a lot! Special thanks to Fabrice Wendling for welcoming us. Thanks to Pascal, Julien, Maxime and Mahmoud for your time and knowledge shared. My stay in Rennes with the entire Fabrice's group was a refreshing and inspiring experience for this work. Thank you all.

I have a great family by my side that believe in me more than myself: mum, dad, I wouldn't be where I am if it wasn't for your effort and hope. Ferran, a brother who has proven to be there in any situation and a brother that gives me the extra energy I need to achieve anything I propose, like finishing this project with proud. Camila, even though you are far away this year, you supported me a lot to make this happen. Thanks for always being there. Thanks, family, I love you a lot. And here I include Paula, who is like a sister for me. Thanks for sharing every single moment of these years of university. We have proved that together we can deal with anything. I'm excited to see what else we can do in the future, together. I love you a lot, Paula. Thanks for all the positive energy you give to me every day.

Finally, I want to thank two special people I have met in the past year. Thanks, David, you given the best motivation ever, super positive and unconditional, you are star for me, you know it.
And special thanks to Hervé Viens, even though he is at the other side of this planet, I could feel really close all his love and support. You have been really present during this year, and you will always be. Thanks.

Summary

In the present study we present a new modeling approach of a whole-brain network model based on a combination DTI-driven anatomical connectivity of the brain and Jansen and Rit neural mass model. We also propose an approach to personalize such brain network model with subject specific EEG and MRI data. We study the structural and functional relationship and the inter- and intra-subject variability for two healthy patients with different conditions, eyes open and eyes closed resting-state EEG. The personalization is based on a comparison of functional connectivity estimates between simulated and real data to fit the parameters of the model. The vision of this study is to generate a proof of concept that which such models we can personalize virtual brains models in order to customize treatment for neurological diseases.

Keywords

Brain Network Model, Neural Mass Model, Structural Connectivity, Functional Connectivity, Subject variability.

Index

List of figures

List of tables

MAIN SECTION

1. INTRODUCTION

Personalization has become a standard practice in medical diagnosis, treatment and product design. Healthcare industries are investing on it due to the clear impact that individual variability has on the effectiveness of the therapy. In this work we propose a first step towards a solution to these personalized-oriented practices related to neurological conditions. We present subject-specific brain network models (BNM) based on a combination of noninvasive electrophysiological and neuroimaging techniques (e.g., MRI, EEG and Diffusion Tensor Imaging, DTI) and computational models of brain activity.

The present study is an excellent starting point to gain insight into the effects of different neurological therapies such as transcranial stimulation (tCS, TMS) or drugs on individual subjects, and thus could to lead to the development of personalized treatment strategies.

The human brain is an inherently dynamical system that can be defined as a network of networks, deployed at multiple scales and with different levels of complexity. Multiple studies in theoretical and computational neuroscience have developed whole-brain network models (Bansal et al., 2018; Cabral et al., 2014; Deco et al., 2011) to explore the relationship between the brain function and its underlying connectivity. This increased interest in finding the origin behind the structure-function relationship has led to a new developing field known as Network Neuroscience (Bassett & Sporns, 2017), which relies on network theory to study the brain across its multiple scales and complexities.

In this framework, the nodes of the BNM are mathematical equations that describe the temporal electric brain activity. Traditionally, two main classes of models have been used to represent the electrical brain dynamics.

On one hand we have the spiking neuron models such as the integrate-and fire and more detailed models like Hodgkin-Huxley (Hodgkin & Huxley, 1990). These models are appropriate for single cell recordings in animals or brain slices, but their state variables do not directly capture the functional activity recorded with macroscopic level techniques such as EEG, MEG or mesoscopic LFP measurements.

In contrast, neural mass models (NMM) are more relevant when modeling brain activity at a larger spatial and temporal scale since they describe the mean activity of whole neural populations, represented by their averaged firing rates and membrane potentials. Despite the fact that they are less detailed, they are still able to represent the physiology of the brain: their parameters emerge from microscopically measurable quantities, such as dendritic time constants and mean excitatory/inhibitory post synaptic potentials. Moreover, they provide connections to macroscopically measurements such as EEG.

The most used NMM are modifications of Wilson and Cowan oscillators or Jansen and Rit model (Jansen et al, 1995, 1993). There are some other studies such as (Cabral et al., 2012; Cabral et al., 2014) that use simpler models such as Kuramoto oscillators to simulate the electric brain activity, but they lack a direct physiological meaning. More detailed versions are emerging rapidly (Wendling et al., 2012, 2016).

Depending on the complexity of the model, network nodes can represent either single cells, cortical patches, or whole brain areas. The decision of the scale depends either on the data available or the scenario that we want to model. See an extended review by Breakspear (Breakspear, 2017) for a detailed discussion on the choices for the dynamical equations.

Accordingly, network edges are also defined to describe appropriately the links between nodes. If there's subject specific structural connectivity data available, network edges are commonly derived in proportion to the number of white matter tracts between brain areas (when modeling whole-brain dynamics), usually using the well-known human connectome(Hagmann et al., 2007). However, when this data is not available researchers have substituted the connectivity data for functional connectivity or have used available datasets of generalized structural connectivity, as we are doing in our approach.

Bansal and colleagues (Bansal et al., 2018) present a review of the latest work using personalized brain network models to study the structure-function relationship in human brains. However, most of the studies cited in that review are based on static network structures with fixed connection strength and time delays, failing to reproduce some meaningful features of brain dynamics.
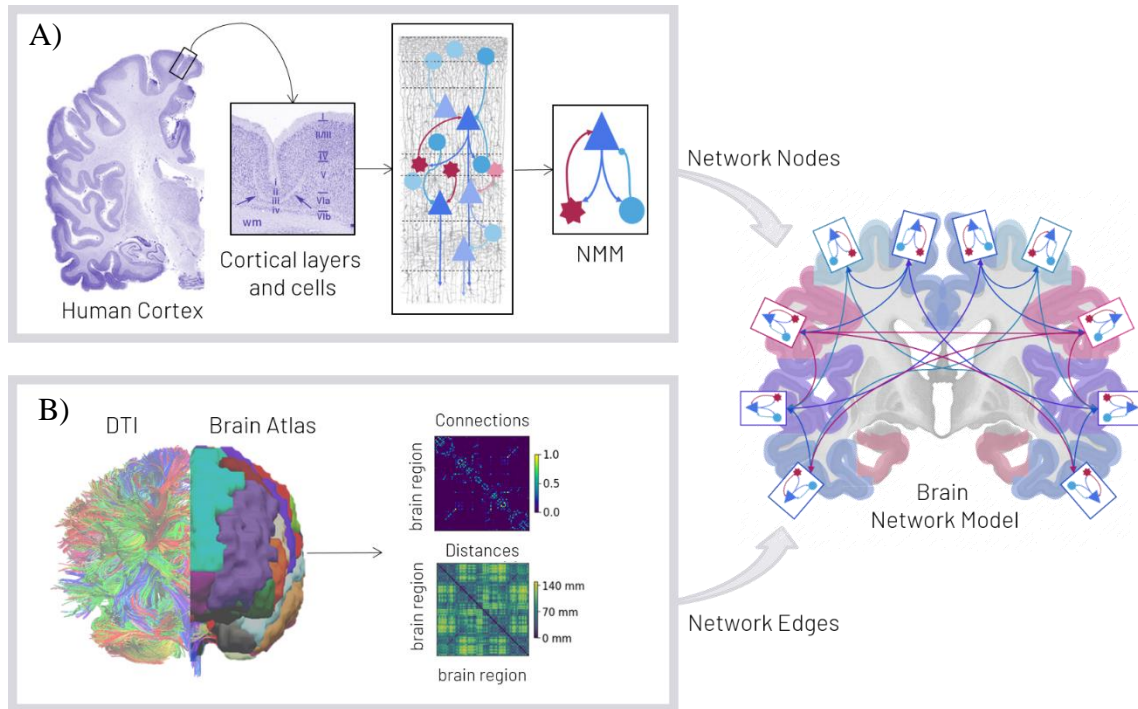
Figure 1. Brain Network Model. *A) Network nodes symbolize brain areas whose electric activity is described by Jansen and Rit NMM, a set of mathematical equations based on the abstraction of the human cortex physiology. **B)** Integration of real data to represent either the connection strength between nodes (derived from DTI) and the transmission delay (proportional to the distance between AAL areas).*

In this work we propose a to fit the *coupling gain* (connection strength) and *mean conduction velocity* with subject-specific EEG and MRI, making our BNM sensitive to individual variability, using an extension of Jansen and Rit neural mass model to represent the network nodes.

We chose to use Jansen and Rit NMM here since it is able to simulate mesoscopic and macroscopic activity of the brain and it can be tuned to simulate either physiopathological electric signals (Wendling et al., 2000; Wendling et al., 2010; Cabral et al., 2012) or its possible response to interventions like transcranial stimulation (tCS, TMS) (Kunze et al., 2016; Merlet et al., 2013; Molaee-Ardekani et al., 2013; Muldoon et al., 2016) or drugs (Kurbatova et al., 2016; Liang et al., 2015).

Driven by the fact that we are performing the fitting of the parameters resting-state EEG form the entire brain (unlike intracortical EEG where we record brain patches), each of the neural masses represents a brain region defined by a parcellation scheme taken from available atlases. Consequently, network edges represent the anatomical links (structural connectivity) between each of the brain areas. Moreover, the presented BNM also considerers the time delays between the interconnected regions of the brain to be proportional to the structural distance between them (Cabral et al., 2011), see Figure 1 for an illustrative scheme of how the presented brain network model is built.

The coupling gain and mean velocity are the parameters of our model that are used to include connectivity data in the neural mass model, as derived from DTI. These parameters, coupling gain and velocity, scale the overall connectivity strength across nodes and, together with the measured distance between parcellated regions of the brain, the time delays between regions. The decision why we choose to fit these two parameters is because they come from an averaged representation across different subjects (not the ones the MRI and EEG were recorded from), are the least known or most variable parameters across subjects and address directly global phenomena we will use to optimize, that is EEG. (Figure 2).
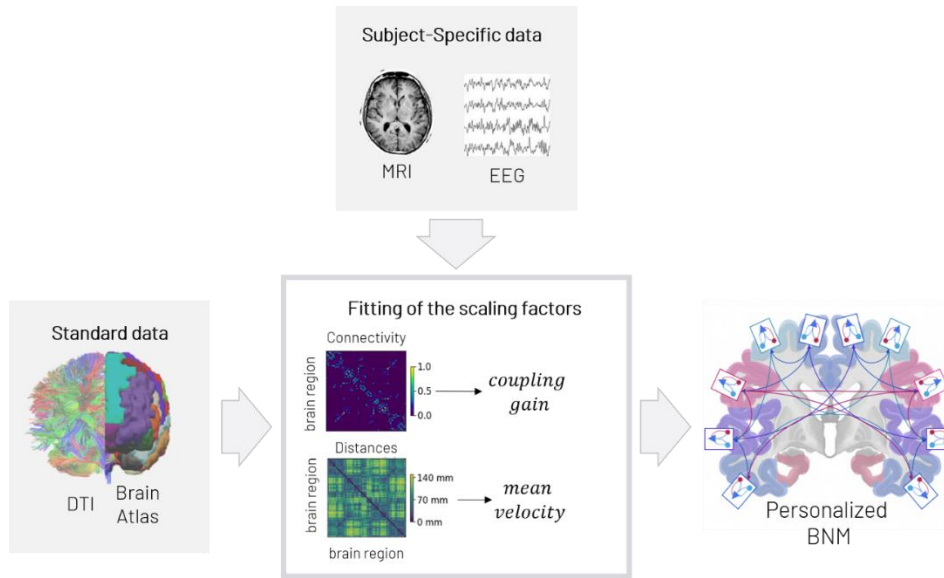
Figure 2. Personalized Brain Network Model. *Customization of the brain network model based on non-invasive subject-specific data (EEG, MRI). The personalization is based on the fitting of the parameters that scale the generalized human-brain data we use to build the BNM.*

The fitting process is based on the correlation between the functional connectivity (FC) profile of the simulated brain areas and the FC profile of the inversion of the subject's

EEG on a 3D mesh of the brain reconstructed from its own MRI and averaged among the same parcellation that we use to define the scale of the model.

This FC estimate is based on (Cabral et al., 2014), which takes into account the fact that resting state BOLD signal fluctuations are driven by slow modulations in the power (and therefore, amplitude) of brain oscillations in different frequency ranges (Figure 3). Studies mentioned in (Cabral et al., 2014) show that simultaneous recordings of EEG-fMRI point to an inverse correlation between BOLD signals and the power of alpha (8-14Hz) and beta (13-30Hz) brain waves (Mukamel et al., 2005), which might be related with the deactivation and decreased metabolic rate. Moreover, recent MEG studies of resting-state activity have found slow fluctuations in the power of the oscillations that correlate across distant brain areas, especially when considering beta (13-30Hz) oscillations.

In general, recent studies indicate that resting-state functional connectivity in BOLD responses corresponds to a spatially structured amplitude modulation of neural oscillations in the alpha-beta range (8-30Hz).
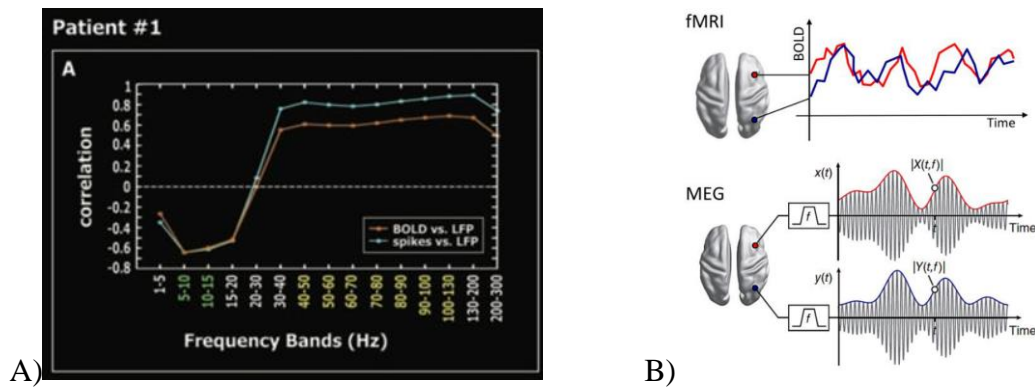

A)   B)

Figure 3. BOLD signals and fMRI Functional Connectivity. *A) Correlation of the different LFP predictors with the average fMRI BOLD signal in Heschl's gyrus (orange) and with the spile predictor (cyan) as a function of frequency band (Figure from* (Mukamel et al., 2005)*). B) (Top) fMRI functional connectivity is assessed as the correlation between the BOLD signals recorded at different locations. (Bottom) Resting-state functional connectivity in MEG, assessed by first band-pass filter the MEG signal, extracting the amplitude envelope (red and blue lines) of the underlying carrier frequency (black). This strategy results in a set of frequency-specific FC (Figure from (Hipp et al., 2012).*

This parameter fitting approach based on FC profiles correlation has been already shown to be significant when comparing brain network models with MEG real signals. Indeed, in the work done by (Cabral et al., 2011) it was shown that there is an optimal fit with resting-state BOLD functional connectivity occurred in a critical range of model parameters of interconnected Kuramoto oscillators.

In this work, we use our biophysically realistic BNM to explore how slow and structured amplitude envelopes of band-pass filtered signals are generated spontaneously and vary with time and position. We also study how well the extension of Jansen and Rit's model, combined with standard structural data, fits subject specific data based on FC profiles. Finally, we will explore how this fit depends on model parameters and on different subject data.

2. MATERIALS AND METHODS

2.1 Subject data: EEG and MRI

In this work we used EEG and MRI data of two different healthy subjects, labeled as subject 55 and subject 60. The data was collected for the purpose of another study carried out at BIDMC (Harvard Medical school), but the PI (Dr. Santarnecchi) gave us permission to use it in this work. EEG data was recorded during resting state for 2 minutes and for two different conditions, eyes closed and eyes open (sampling rate 1000 Hz, 64-channels, for other information see Appendix A). MRI structural data was acquired using T1-weighted images (256 x 256 x 256 voxels).

2.2 From MRI to electric brain model

In this section we introduce the steps followed to obtain the electric field distribution in a 3D brain model of a specific subject (Figure 4). This electric brain model will be necessary to perform the source estimation of the resting state EEG from the same subject since our goal is to compare model and measured electrical activity at the cortical level. For this purpose, we use a personalized cortical mapping algorithm (CM) to map electrode space data to cortical mesh space following an approach based on the reciprocity theorem (G. Ruffini, 2016; Miranda et al., 2012). We first calculate the electric field (E-field) distribution in the brain by injecting current through the same electrodes used in the EEG recordings (this in embodied in the reciprocity theorem as discussed in section 2.4).

The electrostatic potential (V in volts) in the brain induced during transcranial current stimulation can be obtained from the Laplace's equation with appropriate boundary conditions:

$$\nabla^2 V = 0$$

From it we can obtain the electric field vector ($\vec{E}$, in volts per meter) anywhere in the brain:

$$\vec{E} = -\vec{\nabla} V$$

The calculation of Laplace's equation requires knowledge about the geometry of head tissues, the geometry of the electrodes, the electrical conductivity of the tissues (σ in Siemens per meter) and the current injected in each electrode (I in Ampères).

An analytical solution of this equation is only possible in simple head geometries (as in spherical head models) so numerical methods are commonly employed. A frequently used method is the Finite Element Methods (FEM) (Feischl, 2017). In this method, the geometry is discretized into simple geometrical shapes (usually tetrahedra for 3D models), finite elements, forming the finite element mesh. Within each element, it is assumed that the distribution of the solution to Laplace's equation is a linear combination of simpler shape functions (usually second order polynomials are used). With this approximation it is possible to show that the distribution of V within each finite element can be obtained by solving a system of linear equations.

In this work, a software package (COMSOL Multiphysics version 5.3a) was used to implement the finite element method and perform the E-field calculations.

The geometry of the head model created in COMSOL was obtained from MRI data. The T1 weighted image was segmented into scalp, skull Cerebral Spinal Fluid (CSF), air pockets, cerebral grey matter (GM) and cerebral white matter (WM).

Segmentation was performed using three different software tools: MARS (*https://www.nitrc.org/projects/mars/*) and Freesurfer (*https://surfer.nmr.mgh.harvard.edu/*). Triangulated surface meshes of these tissues were created using *iso2mesh* (Fang et al, 2009), a MATLAB toolbox (*http://iso2mesh.sourceforge.net/cgi-bin/index.cgi*)(Fischer et al., 2017). Models of the electrodes used in the EEG recording (cylindrical electrodes 1cm radius, 3mm thickness) were placed on the scalp's surface according to the positions defined in the 10/10 EEG system. Those positions were defined based on manually placed anatomical landmarks (inium, nasium and pre-auricular left and right points).

After generation of the surface meshes for all the tissues and electrodes the finite element volume mesh was created using *iso2mesh* (256 x 256 x 256 tetrahedral elements). The finite element mesh was then imported into COMSOL where tissue conductivities were assigned (0.33 S/m for the scalp, 0.008 S/m skull, 1.79 S/m CSF, 0.4 S/m GM, 0.15 S/m WM and 10^{-5} air) (Fischer et al., 2017). The electrodes were represented as conductive gel (4 S/m).

In order for the CM algorithm to be implemented, E-field calculations had to be performed for every bipolar montage with Cz as the cathode ($-1mA$) and each of the other electrodes as anodes ($+1mA$). All calculations were performed in COMSOL using second order finite elements and using an iterative method to solve the system of linear equations (geometric multigrid solver). A typical calculation took 7 min in a computer with 16 GB of RAM and an Intel Core i7 CPU.

After each calculation we exported the component of the E-field normal to the cortical surface ($E_n = \vec{E} \cdot \vec{n}$, where $\vec{n}$ is a vector normal to the cortical surface and pointing inwards).

The final step was to downsample the grey matter surface mesh and its electric field distribution over the surface to a 25% (~40 000 nodes) of its original size. This step was necessary in order to make the CM inverse solution viable from a computational resources point of view (memory). This reduction was performed using *iso2mesh*.
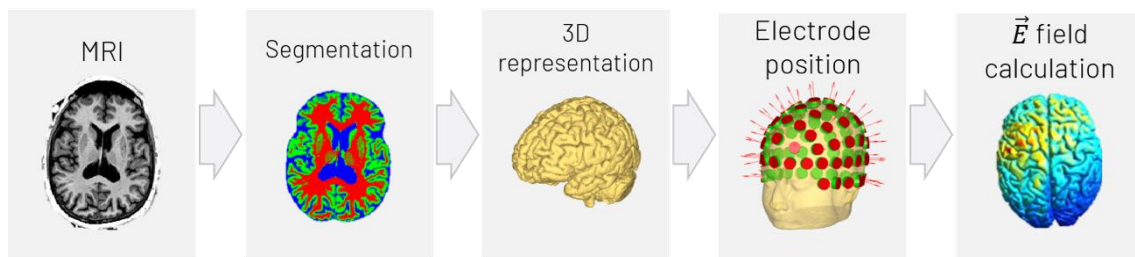

Figure 4. From MRI to $\vec{E}$ field model. *Pipeline to generate a personalized electric brain model from the subject's MRI.*

In what follows, we will be using the grey matter brain mesh to inverse-map the EEG data since dipole sources in the brain are generally distributed in the grey matter volume.

Recorded EEG activity is also thought to come from the sum of post synaptic potentials occurring on pyramidal cells, oriented perpendicularly to the GM surface.

2.3   EEG pre-processing

The EEG was preprocessed with EEGLAB (*https://sccn.ucsd.edu/eeglab/index.php*) a MATLAB toolkit containing all necessary functions to be able to clean and design an EEG pre-processing pipeline to further perform the cortical mapping inverse problem.

The main steps performed to clean the raw EEG were:
1. Line noise removal: we used the EEG-Clean (*http://vislab.github.io/EEG-Clean-Tools/*) plug-in that uses an iterative version of a method that estimates the amplitude and size of a deterministic sinusoid at a specified frequency embedded in locally white noise. The model is applied in sliding windows to adjust for not stationarity.
2. Reject data by visual inspection: before identifying the channels bad channels (channels that could saturate our cortical inversion), we selected 1 min of recording out of unknown artifacts that couldn't be filtered without losing essential information of the recorded signal. In case that we were processing eyes open EEG, we rejected the eye blinks the same way, by visual inspection.
3. Reject the data channels based on channel statistics: EEGlab provides an automatic detection of bad channels based on the kurtosis and spectrum statistics. With the predefined automatic detection and visual inspection, we detected the channels that need to be rejected so the inverse mapping is not contaminated
4. Interpolate the bad channels. It is well known that the inverse mapping improves its accuracy as more channels are used (Hassan et al., 2014). For this reason and because the computation of the mappers is really time consuming and depends on the number of electrodes, we opted for the interpolation of data in the electrodes that were rejected.
5. The final step was to re reference the data to Cz in order to use the generated electric brain model of each of the subjects, which used the same referencing scheme for electrical stimulation.

2.4   Personalized Cortical Mapping

Cortical mapping (or inverse modelling) consists in finding the dipole distribution on the cortical surface that could generate the EEG pattern. The transformation from voltage space to source space (dipoles) is linear and governed by the Poisson equation, so we just need to find the transformation matrix K (commonly referred as the "lead field" matrix). The following equations are based on the reciprocity theorem derived by H. Helmholtz in 1853. For more information about how the mappers are developed using this theorem see(Ruffini, 2016; Ruffini, 2015).

In short, the reciprocity theorem states that there is relationship between the observed potential difference between two points in the scalp ($V_{ab}^{(1)}$) due to a lone dipole current in the brain ($\vec{J_n}^{(1)}$) in a volume δV. It also states that there's a relation between an imposed stimulation ($I_{ab}^{(2)}$) between these two points and the resulting current density in the brain ($\vec{J}^{(2)}$).

Then, the reciprocity relation is:
$$V_{ab}^{(1)} I_{ab}^{(2)} = -\vec{J}^{(1)} \cdot \vec{E}^{(2)} \delta V$$

From this equation we can derive the voltage V_{ab} at a point b with respect to a point a due to a lone dipole $\vec{J}^{(1)}$:
$$V_{ab}^{(1)} = -\sum_n \frac{\vec{E}_n^{(2)} \delta V_n}{I_{ab}^{(2)}} \vec{J}_n$$

Where n refers to the voxel location ID.

Then we have already the linear transformation we want, where K is the forward mapper:
$$V_{ab}^{(1)} = K \cdot \vec{J}_n^{(1)}$$

The "lead field" matrix K is associated to unitary currents $I_{ab}^{(2)} = 1 \, mA$, so we just need to find the electric field distribution produced by a reciprocal montage at a and b using our head model.

Once we have the forward mapping matrix K, we need to invert the transformation to infer cortical activity from electrode measurements. There are infinite solutions to this problem, i.e., to generate the inverse mapper of K, to go from voltage space to source space (K^{-1}) – the problem is ill-posed. To address it we will use spatial regularization to produce the inverse solution based on a criterion of spatial smoothness derived from the geodesic distance between mesh points of the head model. In this approach, the data and the curvature (which we want to minimize) constraints are treated equally.

We will use the 2D geodesic distance (over the surface of the mesh, $d(x, x')$) across cortical surface points of the geometric representation of the grey matter for each of the subjects. The matrix for regularization then will be:

$$R(x, x') = \delta(x, x') - \frac{d(x, x')^{-2}}{\sum_{x \neq x'} d(x, x')^{-2}}$$

The condition RJ=0 basically states that the value of J at a mesh point should be equal to a local spatial average of its neighbor values, with a particular ($1/r^2$) weighting (others could be used, e.g., gaussian). The weight of this condition is controlled by a parameter alpha.

Finally, the inverse mapping would be done by:

$$J = [K^T K + \alpha R^T R]^{-1} K^T V$$

Where
$$J = K^{-1} \cdot V$$

Once we have the mappers, we can transform the recorded EEG into source space to find the electric distribution of the sources in each of the AAL areas (see section 2.6).

2.5   Extension of Jansen and Rit Neural Mass Model

a) Introduction

The Jansen and Rit model (Jansen & Rit, 1995; Jansen et al., 1993) comes from the abstraction of the physiology of the human cortex (see Figure 1A).
The number of layers, composition, thickness and organization are not the same over the surface of the cortex, divided by small regions where those characteristics are homogeneous and have different functionalities.

The basic cortical physiological unit for information processing are the *cortical columns*, sometimes referred as microcolumn or functional column. This statement comes from a columnar hypothesis which states that the cortex is composed of discrete, modular columns or neurons, characterized by a consistent electrical and functional profile. Each of these columns contains populations of neurons, 80% excitatory pyramidal cells and 20% of excitatory and inhibitory interneurons, contained in a $300 - 500 \mu m$ patch displaying similar electrical activities (Lodato et al., 2015; Mountcastle, 1997).

Jansen and Rit model simulates a population of pyramidal neurons that receive excitatory and inhibitory feedback from subpopulations of interneurons residing in the same column and excitatory input from other columns or from subcortical regions like the thalamus.

As mentioned before, we are using NMM since they have the ability to represent macroscopic measurements of the brain. The electric potential generated by an individual neuron is far too small to be picked up by EEG or MEG. EEG reflects the summation of the synchronous activity of thousands or millions of neurons that have similar spatial orientation, and pyramidal neurons are thought to produce most of the EEG signal because they are well aligned and can fire together.
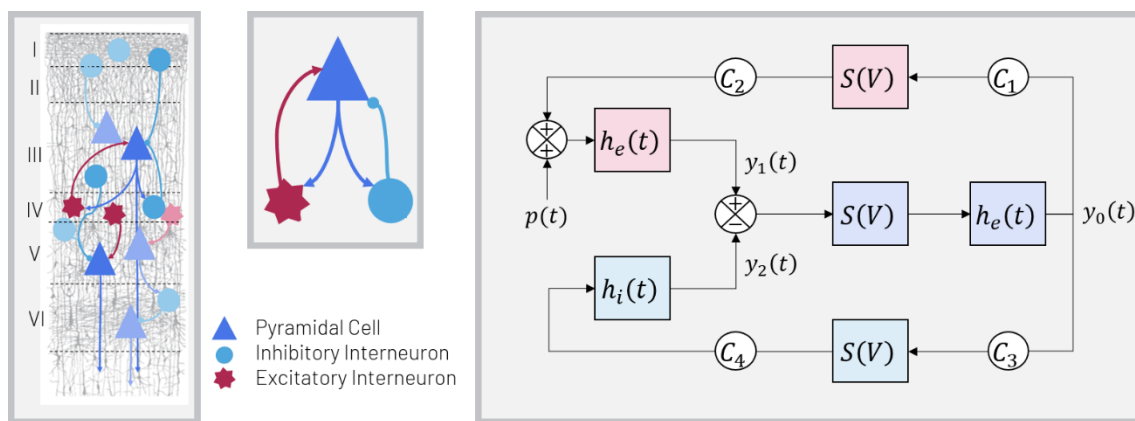

Figure 5. Jansen and Rit NMM. A) *Representation of each of the subpopulations of the model in the cortical layers.* B) *Abstraction of A) and schematic representation of the NMM.* C) *Block diagram representing the equations that governing the model.*

b) Jansen and Rit model of cortical columns

Jansen and Rit developed a model based on the previous work of Lopes da Silva (Lopes da Silva et al. 1974), which developed a model for the thalamus, and based on the PSP transformation that van Rotterdam developed (van Rotterdam et al., 1982).

A schematic representation of the model is shown in Figure 5. The main population are the pyramidal cells located in the layer V of the cortex (represented by triangles and violet color). They receive inhibitory inputs from a sub-population of interneurons, dendrite targeting cells like bitufted, bipolar and double bouquet cells (blue circles in the illustration). Actually, the excitatory feedback must be considered as coming from pyramidal neurons themselves (from other cortical layers, III and VI) more than from genuine excitatory interneurons, which are not numerous in the cortex (red star-shaped figures).

The excitatory input is represented by an arbitrary firing rate $p(t)$ that we model as noise accounting for a non-specific background activity. This input could be also modeled as an impulse function simulating a flash or signal from other regions like the thalamus (Merlet et al., 2013). In section 2.5.d we overview the stability of the model based on this certain parameter.

In Figure 5C the C_i constants represent the interactions between the three types of sub-populations (see table 1 for the biological meaning of each of the constants in the model and the standard values) and their values are based on several neuroanatomical studies where they estimate these constants by counting synapses.

Parameters	Interpretation	Value
A	Maximal amplitude of EPSP	3.25 mV
B	Maximal amplitude of IPSP	22 mV
a	Time constant of average EPSP	100 Hz
b	Time constant of average IPSP	50 Hz
C	Connectivity constant	135
C_1	Connectivity constant from pyramidal (Pyr) to excitatory (Exc) populations	C
C_2	Connectivity constant form Exc to Pyr.	$0.8 \cdot C$
C_3	Connectivity constant from Pyr to inhibitory (Inh) populations	$0.25 \cdot C$
C_4	Connectivity constant form Inh to Pyr.	$0.25 \cdot C$
v_0	Potential when 50% of firing rate is achieved	6 mV
e_0	Half of the maximum firing rate	2.5 Hz
r	Slope of the wave-to-pulse function at v_0	0.56 mV^{-1}
$p(t)$	Excitatory input noise (positive mean gaussian white noise)	$\mu = 90 pulses \cdot s^{-1}$ $\sigma = 30\ pulses \cdot s^{-1}$

Table 1. Parameters, interpretation and values of the original model to produce alpha oscillations.

Each of the populations is characterized by two different type of boxes, wave-to-pulse $S(v)$, and pulse-to-wave, $h_{e,i}(t)$ functions, which link the two state variables of the model: average membrane potentials, $y(t)$, and average firing rates, $x(t)$. These boxes have been previously designed by van Rotterdam (van Rotterdam, Lopes da Silva, van

den Ende, Viergever, & Hermans, 1982b) to reproduce the two essential characteristics of real post-synaptic potentials: shape and excitatory/inhibitory ratios.

The $S(v)$ box, also called "pre-synaptic" box, introduces a nonlinear component that transforms the average membrane potential of a population ($y(t)$ in volts V) into firing rate ($x(t)$):

$$S(V) = \frac{2e_0}{1 + e^{r(v_0 - v)}}$$

The pulse-to-wave box, or post-synaptic box, converts the average rate of action potentials constructing the input of a population into an average post-synaptic potential (PSP). This filtering process is introduced as a second order differential linear transformation:

$$\ddot{y}(t) = Aaw(t) - 2a\dot{y}(t) - a^2\, y(t)$$

where $w(t)$ is the output of the sigmoid function $S(V)$. This second order differential equation can be decomposed in a system of two equations,

$$\dot{y}(t) = z(t)$$
$$\dot{z}(t) = Aaw(t) - 2az(t) - a^2 y(t)$$

There are three main state variables in the system, the average membrane potential of each of the subpopulations of the system, y_0 for the pyramidal cells and y_1, y_2 for the excitatory and inhibitory interneurons, respectively.

Then, the Jansen and Rit model can be described with a set of six differential equations, each pair corresponding to each of the populations:

$$\dot{y}_0 = y_3(t)$$
$$\dot{y}_3(t) = AaS\big(y_1(t) - y_2(t)\big) - 2ay_3(t) - a^2 y_0(t)$$
$$\dot{y}_1(t) = y_4(t)$$
$$\dot{y}_4(t) = Aa\{p(t) + C_2 S\big(C_1 y_0(t)\big)\} - 2ay_4(t) - a^2 y_1(t)$$
$$\dot{y}_2(t) = y_5(t)$$
$$\dot{y}_5(t) = BbC_4 S\big(C_3 y_0(t)\big) - 2by_5(t) - b^2 y_2(t)$$

Where h_e stands for excitatory and h_i inhibitory post-synaptic boxes and $y = y_1 - y_2$ is the membrane potential form the main family of neurons, the output (y) we will be using to represent the artificial signal for each of the areas.

c) Connecting multiple Jansen-Rit populations

In order to explore the hypothesis that visual evoked potentials are due to an interaction between cortical columns, Jansen and co-workers proposed a model in which two populations were coupled (Jansen & Rit, 1995).

The purposes of this section are 1) to establish the general expression of the set of ODEs that describe a new model of multiple coupled populations and 2) to explain how the generalized structural data and special data are incorporated in the model.

We are basing this modification of the original model on the assumption that all the connections between columns are from pyramidal to pyramidal population and thus are always excitatory. The average pulse density of action potentials from the main cells of one population, $x(t)$, is used as an excitatory input to another population of neurons. However, as neuronal populations represent distinct and distant cerebral areas, new parameters are introduced to account for the structural connection among the areas and the delays associated with these connections. For simplicity, we are also assuming that the same cortical column model can be used for all the cortical areas of the brain, considering that the basic neuronal architecture of the cortex is similar throughout its areas.

Inspired by the work developed by Wendling and co-workers (Wendling et al., 2000; Wendling et al., 2010; Wendling & Chauvel, 2008) , a gain constant K^{ij} is used to define the degree of coupling between population i and j. In their work, the K constant is usually fixed in a range where they obtain the desired output, ignoring the physiological meaning of the connections.

At this point is where our new extension of the model introduces a DTI-driven connectivity matrix to connect the Jansen and Rit NMMs derived from the so called structural connectome (Hagmann et al., 2007), such as the work done by (Kunze et al., 2016). In our case, K is given by the normalized structural connectivity matrix scaled by a factor G, the first of the free parameters of our BNM (Figure 6). See section 2.6.d for an overview of the stability of the system as a function of this parameter.
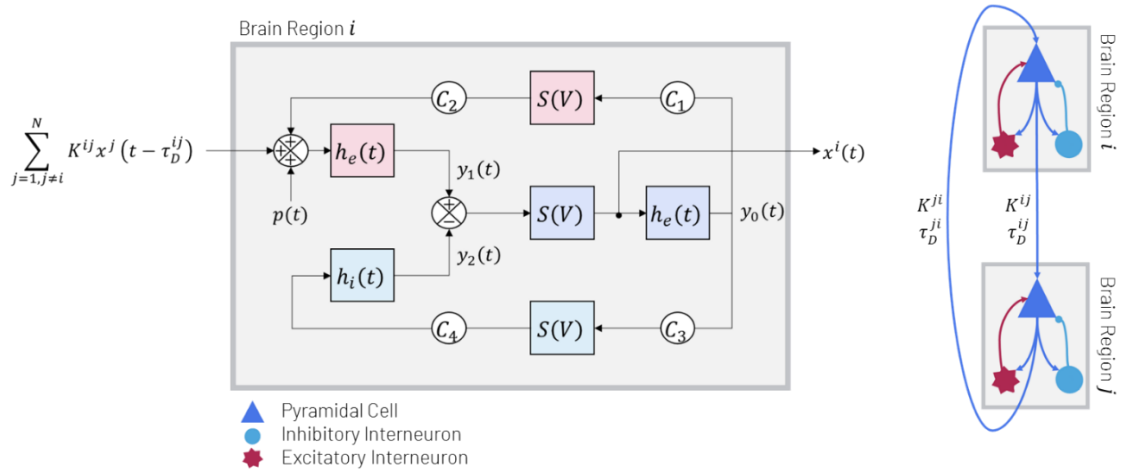

Figure 6. Extension to coupled Jansen and Rit NMMs. *On the left, the block diagram where the components out of the box represent the extension to the original model. On the right, the two parameters of the model that are scaled with real data to represent the structural connections between the areas.*

In the work done by Wendling and co-workers (Wendling et al., 2000; Wendling et al., 2010; Wendling & Chauvel, 2008), they represented the time delay as another pulse-to-wave box as done by (Jansen & Rit, 1995), but that was inconsistent with a physiological representation of the model and, moreover, added two more differential equations per connection, increasing its dimensionality. Furthermore, the time constant they use to represent the delay was dependent on the number of areas involved in the synaptic transmission between known physiological pathways. In case we want to model specific

information processing pathways like visual or language processing interconnected areas, this approach would be appropriate. In our case, when describing whole brain networks based on the structural connection among areas with the goal of comparing model outputs to resting state EEG, this approach becomes inconsistent.

Here we propose a simpler and alternative representation of the time delay, proportional to the Euclidian distance (D_e) between the center of mass of the aforementioned AAL areas, and the conduction velocity v, $\tau_D = D_e/v$ (Figure 6). For simplicity, this conduction velocity is assumed to be homogenous across the brain (Deco et al., 2009).

The final equations used to simulate the brain dynamics in a brain region are:

$$\dot{y}_0(t) = y_3(t)$$
$$\dot{y}_3(t) = AaS\big(y_1(t) - y_2(t)\big) - 2ay_3(t) - a^2 y_0(t)$$
$$\dot{y}_1(t) = y_4(t)$$
$$\dot{y}_4(t) = Aa\left(p(t) + C_2 S\big(C_1 y_0(t)\big) + \sum_{j=1,\, j \neq i}^{N} K^{ij} x^j \left(t - \tau_D^{ij}\right) \right) - 2ay_4(t) - a^2 y_1(t)$$
$$\dot{y}_2(t) = y_5(t)$$
$$\dot{y}_5(t) = Bb(C_4 S(C_3 y_0(t))) - 2by_5(t) - b^2 y_2(t)$$

The AAL template (Tzourio-Mazoyer et al., 2002) was used to parcellate the brain originally into 90 regions, but we were restricted to reduce the parcellation to 78 cortical areas according to (Achard, 2006; Gong et al., 2009). We performed such reduction because we use subject specific 3D grey matter meshes of each of the subjects and when performing the automatic parcellation into the 90 AAL atlas, some of the subcortical areas are not represented in any of the nodes. In the end, the model includes 78 cortical areas, 39 for each of the hemispheres (See Table SI-1 for the names and the represented order of the AAL areas).

d) Bifurcation analysis

When the input noise $p(t)$ is varied smoothly the eigenvalues of the fixed points of the system of equations that describe the Jansen and Rit NMM move across the complex plane leading to Hopf and global bifurcations. For a deep study on the bifurcations that characterize Jansen and Rit model of a cortical column see (Grimbert, 2005). To summarize it, the Hopf bifurcations generate the alpha activity seen in (Jansen et al., 1993) (Figure 7, blue) and the Global bifurcations generate the spike-like epileptic activity that Wendling and colleges (Wendling et al, 2002; Wendlinget al., 2005) use to simulate the SEEG recordings in epileptic patients (Figure 7, orange).
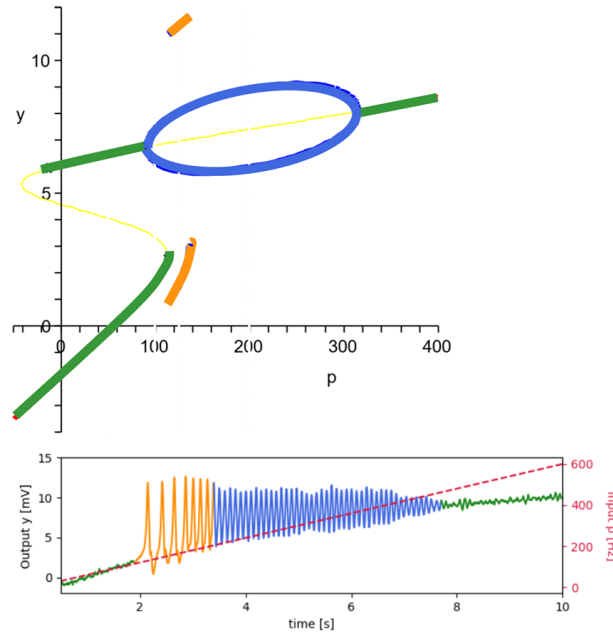

Figure 7. Bifurcation diagram and column activity for increasing values of p. *A) Bifurcation diagram of the system (figure adapted from (Grimbert, 2005)). In yellow we can see the unstable fixed points, in green the stable fixed point, in orange the global bifurcations and in blue the Hopf bifurcations. B) Activity of a single column for increasing values of p.*

When connecting multiple columns (e.g. generating the BNM), we have observed that our system stability also changes in a similar way than when varying the input noise p. See (Ableidinger et al.,2017; Ahmadizadeh et al., 2018; David & Friston, 2003; Kunze et al., 2016) for an extended study on the effect of the coupling factor in different networks of Jansen and Rit models of cortical columns.

We have generated three different BNMs depending on the initial stability ($G = 0$) of the system and on the underlying connectivity:
- Case I, background activity. We have set the initial p value as gaussian noise with a mean (p_μ) of 90 pulses/s and a standard deviation (p_σ) of 30 pulses/s (Figure 7 top).
- Case II, alpha activity. In this case, we set the parameter p similar to the one that Jansen and co-workers (Jansen & Rit, 1995)found to generate alpha activity: $p_\mu = 250$ pulses/s and $p_\sigma = 100$ pulses/s (Figure 7 bottom).
- Case III, same as Case I but it integrates randomized structural and distance matrices (keeping exactly the same coupling weights and distances). This case is

studied to investigate how much of the brain space-time structure is responsible for the for the output of the BNM.

In Figure 8 you can see the effect of increasing values of the coupling gain G on a random node picked form each of the BNM initial cases (We didn't include Case III since at the node level has the same activity as Case I).
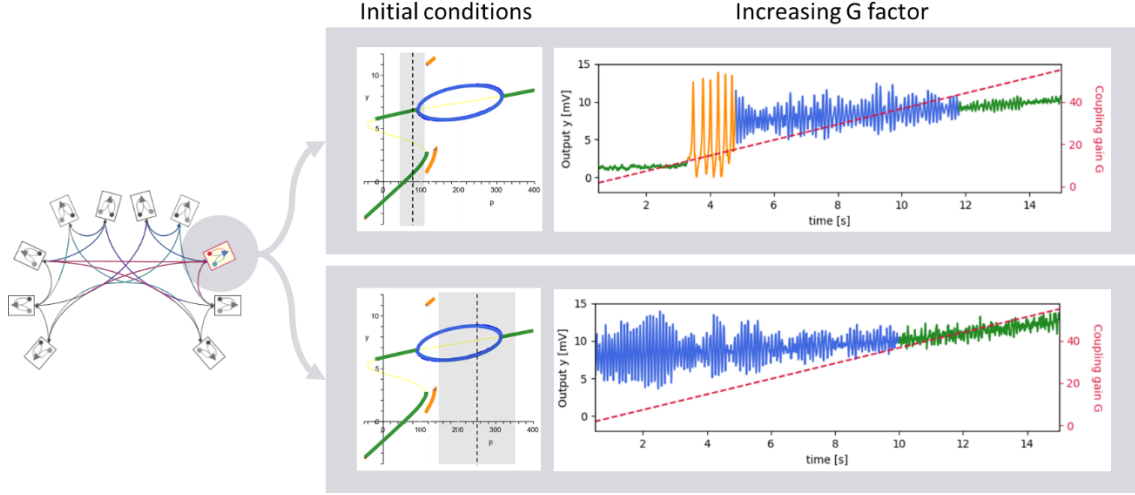

Figure 8. Effect of increasing coupling G in the BNM. *(Top) Case I, the initial input noise is set to generate background activity (green). For increasing G we see that the system hit upon the two bifurcations, global (orange) and Hopf (blue). (Bottom) Case II, the initial conditions are set to generate alpha activity (blue). In this case the system returns to the background activity (green) after being set to start in the Hopf bifurcation.*

As you can see form Figure 8, the system is really sensitive to the coupling factor, leading to a similar behavior as for increasing of the input noise p.

2.6 Functional connectivity estimate

In this section we are going to explain how the FC profile is estimated either from the subject specific data (the corresponding source distribution extracted from the EEG and MRI of each subject and condition) and form the BNM output.

First, we averaged the source distribution of the real data (see sections 2.1-2.4) for each of the 78 cortical areas (mentioned in section 2.5c)). Since we used an automatic parcellation of the brain meshes, the output areas where very heterogeneous, ranging from ~10 to ~1000 number of nodes/area. This lead to an almost equal activity among the 78 brain regions.
In order to deal with this issue and the leakage of the signal between regions generated from the inversion (zero-lag correlations), we removed the common mode of the time series.

What is usually done to remove the zero-lag correlations in source space distribution is to orthogonalize the time courses for each pair of nodes (Hipp et al., 2012). Initially, we account for ~60 EEG channels, so it is impossible to generate 78 independent components. That's why we couldn't perform the orthogonalization and instead we performed the common mode extraction.

Following the pipeline stablished in (Cabral et al., 2012), and considering that BOLD signal fluctuations observed in the brain at rest are associated to slow fluctuations in the power of neuronal oscillations occurring in a particular frequency range (Hipp et al., 2012), we band-pass filtered the real data and the BNM output (time courses of each of the 78 areas) into 5 different frequencies: delta (<4Hz), theta (4-8Hz), alpha (8-14Hz), beta (14-30Hz), gamma (30-58Hz) (following the Recommendations for the Practice of Clinical Neurophysiology: Guidelines of the International Federation of Clinical Physiology (EEG Suppl. 52)).

Then, since the low-frequency component of the envelope fluctuations have been found to be optimal for measuring spontaneous functional connectivity (Hipp 2012, Bro2011), we first extracted the amplitude envelope using Hilbert transform and then low-pass filtered the time courses with a cut-off frequency of 0.5 Hz.

Finally, the Pearson Correlation Coefficient (PCC) was extracted between areas, representing the final FC profile of the BNM and real data.

The last step was to correlate the real and simulated FC profiles and see how well our model fits the real data. This FC-correlation error function was also used to optimize our two parameters, and it is done by comparing the PCC for each pair of parameters G and v. See Figure 9 for a summary of the pipeline followed.
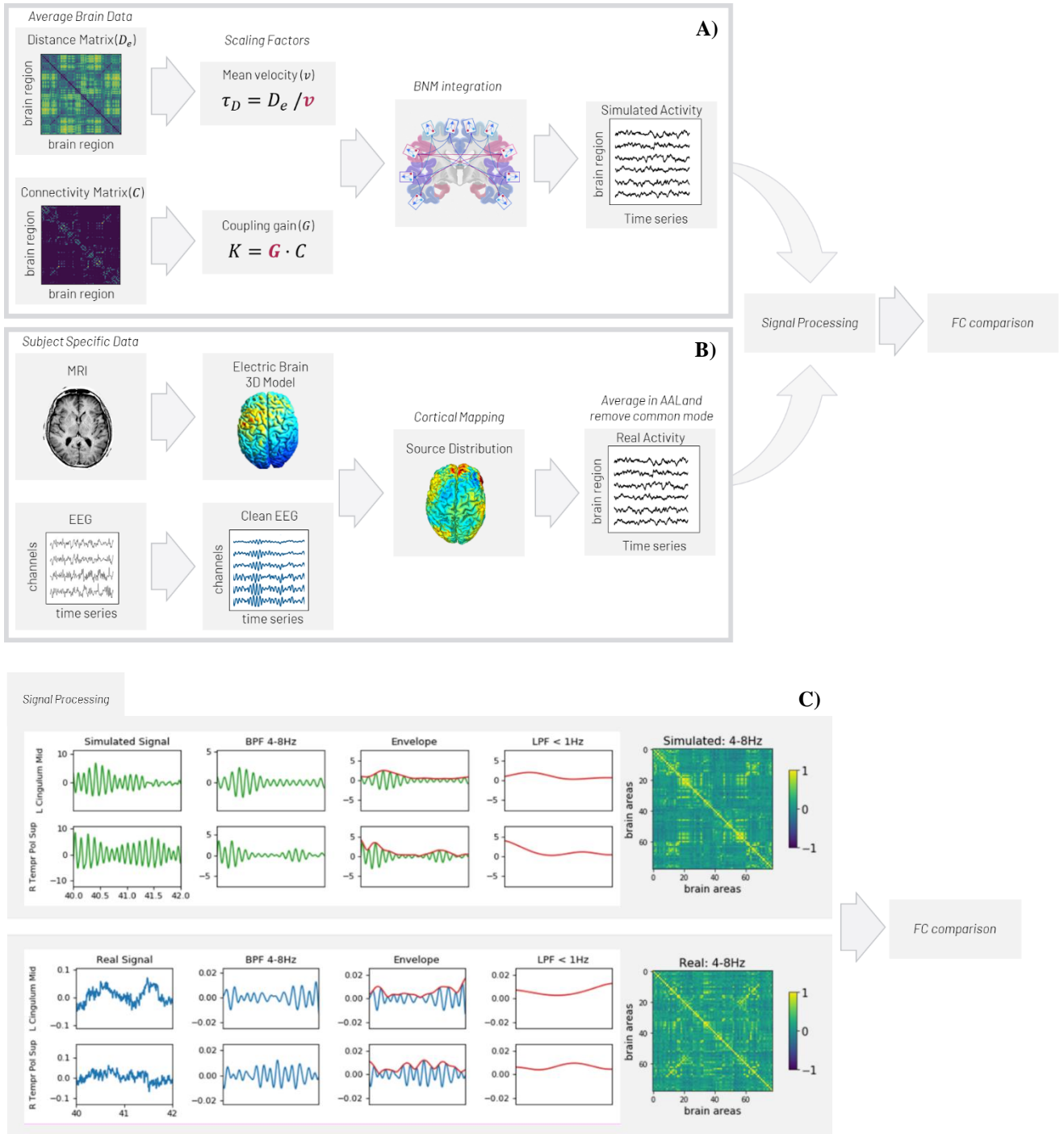
Figure 9. Summary of the pipeline followed. *A) Generation of the simulated brain activity in each of the 78 AAL areas from Standard Brain Data. B) Processing of the real data to obtain the activity for each of the 78 AAL areas. C) Signal processing steps to obtain the FC profile. Note that just one of the five frequency bands is shown.*

3. RESULTS

3.1 Correlation with the underlying connectivity

The relationship between functional and structural connectivity is not trivial and has been subject of investigation for several theoretical and computational research groups over the last decade (Deco et al., 2009; Honey et al., 2007; Ponce-Alvarez et al., 2015). These works have proved using whole-brain network models how the anatomic structure can shape spontaneous brain activity on slow fluctuations, showing consistent patterns of Functional Connectivity.

In this section we show the correlation between the structural connectivity matrix and the generated FC matrix for each of our BNM cases (Figure 10).
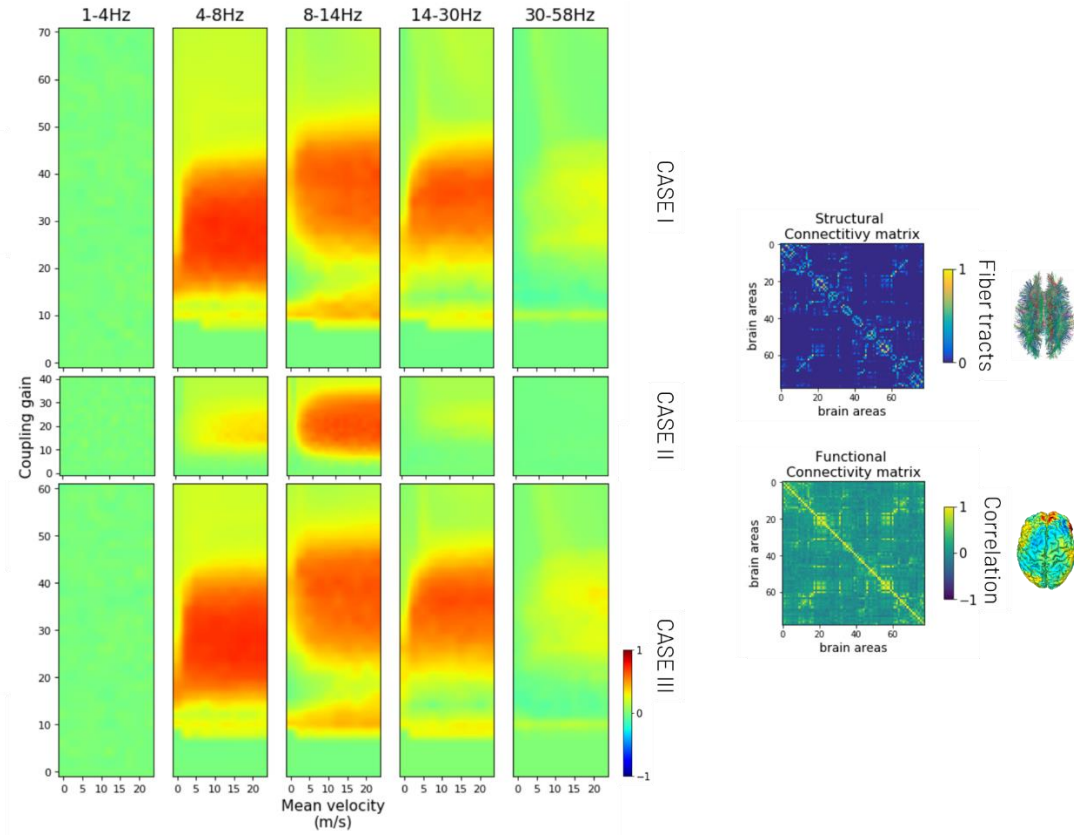
Figure 10. Functional and Structural matrices correlation of the BNM. *(left) Correlation maps between functional and structural connectivity for each of the cases (See Section 2.5d) and pair of parameters G and v. (right) FC profile of the BNM in Case I which as the set of parameters that generate the higher correlation with the structural connectivity matrix: $freq = 4 - 8Hz$, $\rho = 0.74$, $G = 28$, $v = 16m/s$. Note that the parameter range for Case II is lower since it was enough to englobe the system bifurcations.*

In Figure 10 (left) we can see that the underlying structural connectivity of the BNM has indeed a strong effect in the FC profiles, achieving maximum values of $\rho_I = 0.74$, $\rho_{II} = 0.67$ and $\rho_{III} = 0.74$, respectively. Note that Case III has the same initial noise conditions than Case I (See Figure 8) but with a randomized structural and distance connectivity matrices.

The emergence of these correlations is obtained when the coupling gain G is such that the system operates in the bifurcations (see Figure 8). For Case I and III, when $G \sim 10$, is when the system experiences the global bifurcations (Figure 8, orange line, spiking regime), shaping the structural connectivity behind.

The other regime where we observe the highest correlation is when the whole BNM produces alpha activity (Figure 8, blue line, alpha activity, 8-14 Hz), clearly seen in Figure 10 for the Case II in the alpha frequency band. Note that when $G = 0$, for Case II, the system is already operating in the Hopf bifurcation, but we don't start to see the correlation with the structure connectivity until G reaches higher values, which denotes again the high impact of the Structural Connectivity in the BNM.

In Case I (and Case III), for increasing values of G the system goes from background activity, to spiking activity (4-8Hz), to alpha activity (4-14Hz) and finally returns to background (see Figure 8). This variety of frequency oscillations that the system experiences is reflected in the mean correlation of each of the narrow bands. In Case II, since the BNM just creates alpha activity, we just see a higher correlation in the alpha band.

3.2 Correlation with real data

The FC profiles obtained with simulations were compared with the ones from real EEG data (subject 60 with eyes open condition, EO) for a range of model parameters G and v like the previous section. As it can be observed in Figure 11A, the fit between real and simulated FC profiles is really sensitive to the coupling gain G and mean velocity, v. To ensure the significance of the results we have also masked the obtained results with a $p - value < 0.001$ (Figure 11B). Figure 13 shows the correlation maps for the subject 60 eyes closed condition (EC) and subject 55 EO, with Case I BNM.

The model shows the best agreement with reality for similar range of parameters as the ones mentioned in the previous section, where the system operates in the edge of bifurcations (Figure 8). Even though in this case we observe noteworthy differences between Case I and Case III, where in the latter there's no correlation at all with real data. This shows the big relevance of the underlying structural connectivity when comparing to the real data.

We also find in Figure 11 that the mean functional correlations are stronger in theta band (4-8Hz) for Case I and alpha band (8-14Hz) for Case II, with higher values in Case I. This significant difference is due to the higher range of frequency oscillations that Case I exhibits for increasing values of G (See figure 8, where it Case I is shown to reproduce theta, orange line, and alpha, blue line, oscillations).

The FCs, envelope correlation matrices, for each frequency band of real and simulated data obtained where the model showed the best agreement with the real FC estimate (Case I, $G = 30, v = 12 m/s$, freq range $= 4 - 8Hz$) are represented in Figure 12.
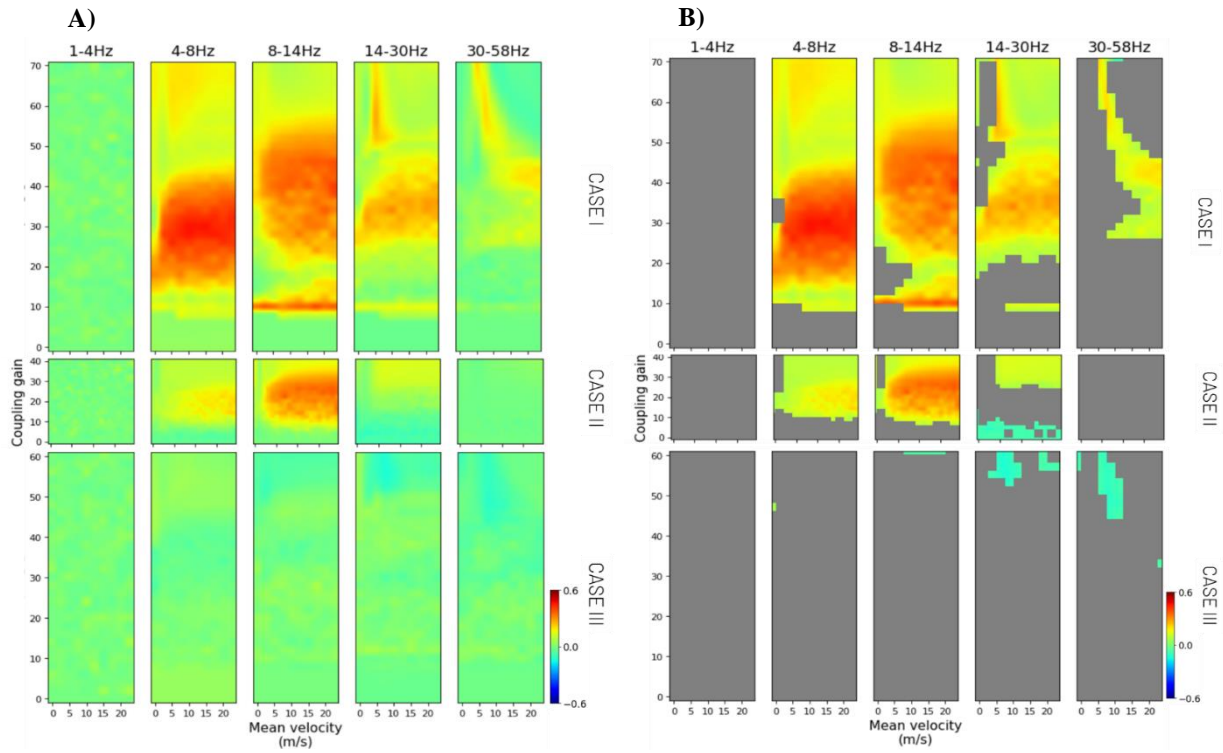
Figure 11. Correlation of real and simulated FC profiles as a function of G and v. *A) Correlation of the simulated FC with the real FC profiles extracted from Subject 60 with EO condition.* **B)** *Same as A) but with a mask of a $p-value < 0.001$.*
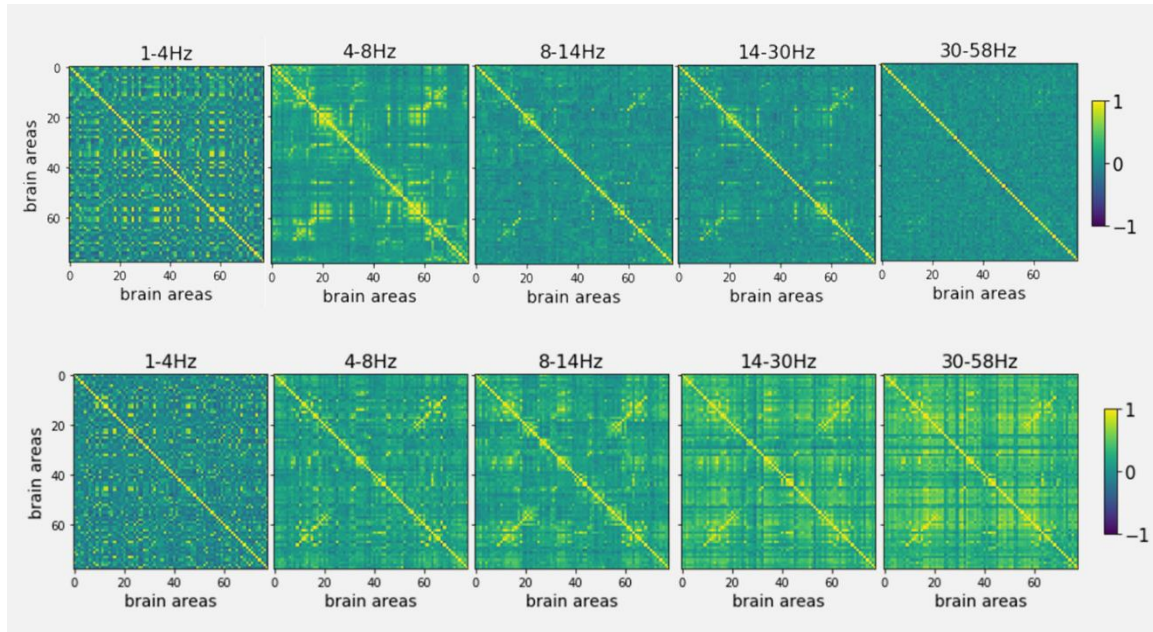

Figure 12. FC profiles for the best parameter fit in Case I. *(top) Simulated FC profiles of each of the studied frequency bands. (bottom) Real FC profiles of subject 60 with EO condition.*
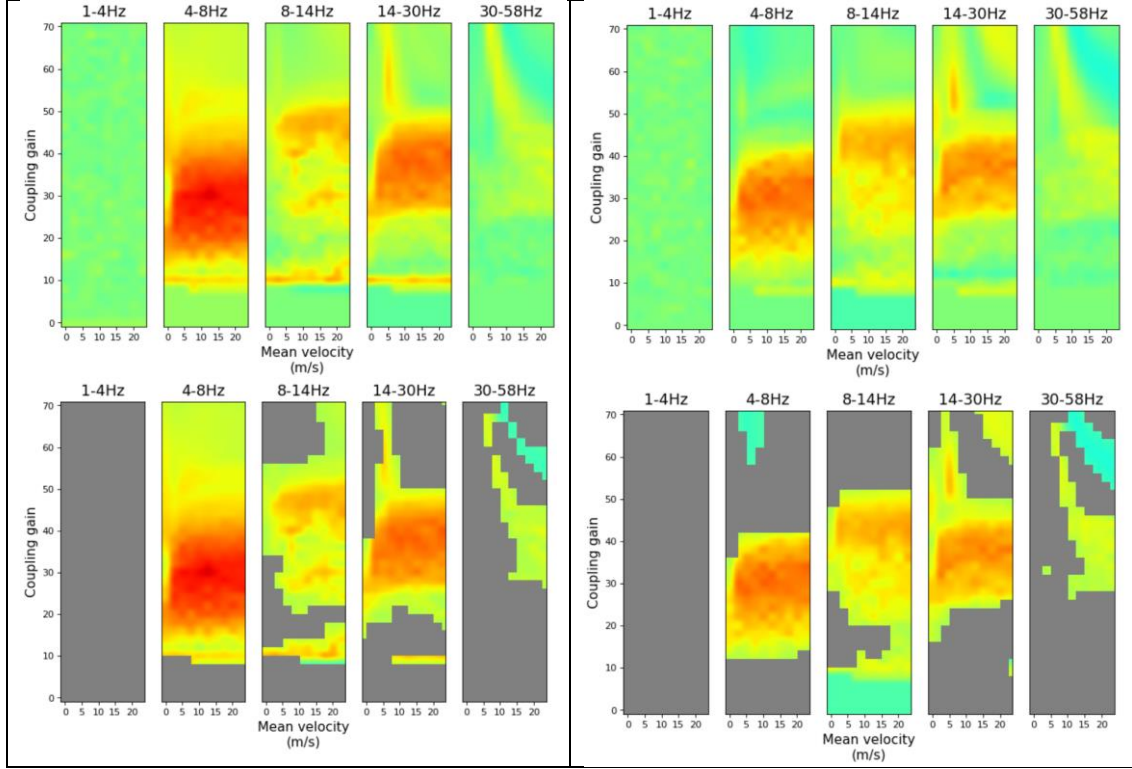
Figure 13. Correlation maps for subject 60-EC and 55-EO. *(top) Simulated FC profiles of each of the studied frequency bands. (bottom) Real FC profiles of subject 60 with EO condition.*

3.3 Subject and condition variability

In this section we compare the same results for each of the subjects (Subject 60 and 55) and conditions (eyes open, EO, and eyes closed, EC) to observe the inter and intra subject variability. Figure 14 shows the mean, maximum and minimum correlation between the BNM – Case I and each of the subjects and conditions. We have chosen to compare with real data Case I BNM for its larger range of neural activity types when varying the G factor.
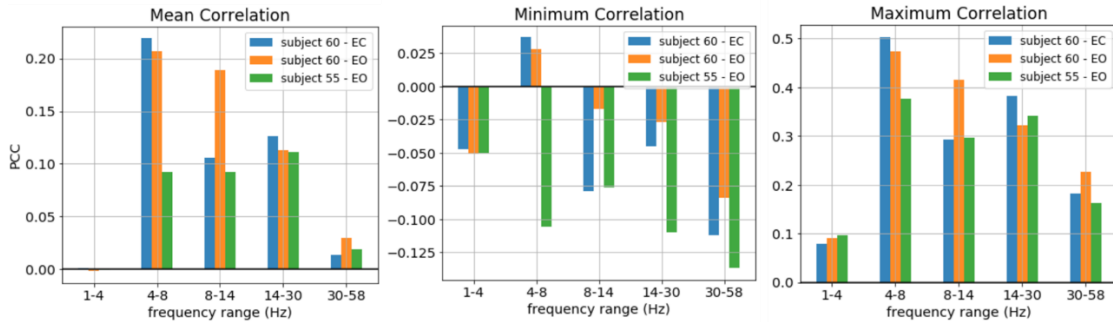
Figure 14. Inter and intra subject variability in the FC profile comparison with the BNM in Case I. *(left) Mean Correlation within subjects and conditions for Case I BNM in each frequency range. (center) Minimum correlation. (right) Maximum correlation.*

As shown in Figure 14 there are significant differences between subject and conditions. In general, subject 60 show higher correlations with the simulated data than subject 55, which has more set of parameters that lead to a negative correlation between FCs.

Moreover, subject 60 has a notably higher mean correlation for alpha and beta frequencies compared with subject 55.

4. DISCUSSION

Relevance of the structural connectivity and coupling gain G

The FC extracted from the BNM proposed in this study show a tight relationship with the underlying structural connectivity (Figure 10, $\rho_{max} = 0.74$), even higher than shown in previous studies (Cabral et al., 2012). The highest correlation occur when the whole-brain model operates at the Hopf bifurcations of the Jansen and Rit NMM. This increased correlation when the model parameters are such that the system operates at the bifurcations can is also found when comparing real FC profiles and simulated FC profiles (Figure 11). It seems to be a common factor of these type of models, since other studies have observed similar outcomes (Cabral et al., 2011; Deco et al., 2009).

Another fact that adds importance to the underlying structural connectivity data is the comparison with simulated activity of Case III (with random distributed structural and distance data). We can observe that, even its FC profiles of Case III are strongly correlated with the underlying anatomical connectivity (Figure 10), they do not show any correlation with real data FC profiles (Figure 11).

The relevance of the structural connectivity observed in the mentioned results, together with the fact that the model stability is really sensitive to the coupling gain, rise the belief that the personalization of the model (fitting of the coupling G parameter) could be improved using subject specific DTI-driven structural connectivity matrix.

Mean velocity of transmission

The model stability has shown lower sensitivity to the mean velocity of transmission for the range of the study $(1 - 20 m/s)$. These results could be enhanced if instead of using the Euclidean distance between the center of masses of each of the AAL regions we could compute the geodesic distance which seems to be more realistic. Such geodesic distance could be extracted from the brain meshes of the subjects, instead of using generalized data.

Further studies regarding parameter fitting of the velocity of could be done. For example, comparing healthy and amyotrophic lateral sclerosis (ALS) patients. It could be investigated if the proposed parameter fitting could be a predictor of the ALS chronic disease, showing an increased correlation for a lower range of v parameter in ALS subjects compared with control.

Positive correlation with BOLD fluctuations

An important fact to take in account is that we have observed a majority of positive correlations in each of the frequency bands when generating the real and simulated FC profiles. This is contradictory with the evidence shown in (Mukamel et al., 2005) and several studies mentioned in (Cabral et al., 2014), which point to an inverse correlation between BOLD signals and the power of alpha (8-14Hz) and beta (13-30Hz) brain waves (Figure 3).

Limitations

There are several limitations we have faced in this project that lead to future improvements if possible.

First, we had not enough parcellated areas. We had a constrain of a 78 cortical regions because the automatic segmentation didn't recognize some of the areas in the subject's head models. We could either change such automatic parcellation and segment each of the areas in homogeneous (regarding the number of nodes) smaller regions. It has been shown that an atlas with approximately 140 brain regions produces a good agreement with experimental data (Proix et al., 2016).

Another clear limitation has been the ratio of number of electrodes and simulated areas. We had just 60 electrodes per subject, thus was not possible to generate 78 independent areas. Moreover, the detailed study of (Hassan et al., 2014) show a clear improvement in accuracy of different Inverse Methods, where the wMNE (similar to the one we are using) shows the best result when accounting for 180 electrodes.

A further study of the effect of the EEG pre-processing has to be done to acknowledge the effects that this cleaning has on the estimated FC profile. It's still unclear if the interpolation of the bad channels could add some noise to the process.

An open door for further studies in virtual brains

This present study is a proof of concept to show that the proposed modelling approach of the BNM (a combination of structural connectivity data and Jansen and Rit NMM) has the potential to represent meaningful features of EEG data. It also shows that the pipeline used to extract the functional connectivity and further correlation between simulated and real data is sensitive to subject's variability and conditions.

Thus, further studies can be done with this modelling approach to gain insight into the effect of neurological therapies such as transcranial stimulation (tCS, TMS) (Kunze et al., 2016; Merlet et al., 2013; Molaee-Ardekani et al., 2013; Muldoon et al., 2016) or drugs (Kurbatova et al., 2016; Liang et al., 2015) on individual subjects, and therefore could to lead to the development of personalized treatment strategies.

Jansen and Rit model is able to simulate either physiological and physiopathological neuronal signals (Wendling et al., 2000; Wendling et al., 2010; Cabral et al., 2012). This also opens the possibility to tune such NMM in order to reproduce different frequency bands, such as epileptic spikes, and perform the same fit of parameters (or other parameters of the model that regulate the excitability of the system, such as A), and observe which parameter range reproduce the best fit with the patient's data to further develop a personalized therapy.

SUPPORTING INFORMATION

#	Left hemisphere	#	Right Hemisphere
1	L Precentral	40	R Temporal Inf
2	L Frontal Sup	41	R Tempr Pol Mid
3	L Front Sup Orb	42	R Temporal Mid
4	L Front Mid	43	R Tempr Pol Sup
5	L Front Mid Orb	44	R Temporal Sup
6	L Front Inf Ope	45	R Heschl
7	L Front Inf Tri	46	R Paracentr Lob
8	L Front Inf Orb	47	R Precuneus
9	L Rolandic Oper	48	R Angular
10	L Supp Motor Ar	49	R SupraMarginal
11	L Olfactory	50	R Parietal Inf
12	L Front Sup Med	51	R Parietal Sup
13	L Front Med Orb	52	R Postcentral
14	L Rectus	53	R Fusiform
15	L Insula	54	R Occipital Inf
16	L Cingulum Ant	55	R Occipital Mid
17	L Cingulum Mid	56	R Occipital Sup
18	L Cingulum Post	57	R Lingual
19	L ParaHippocamp	58	R Cuneus
20	L Calcarine	59	R Calcarine
21	L Cuneus	60	R ParaHippocamp
22	L Lingual	61	R Cingulum Post
23	L Occipital Sup	62	R Cingulum Mid
24	L Occipital Mid	63	R Cingulum Ant
25	L Occipital Inf	64	R Insula
26	L Fusiform	65	R Rectus
27	L Postcentral	66	R Front Med Orb
28	L Parietal Sup	67	R Front Sup Med
29	L Parietal Inf	68	R Olfactory
30	L SupraMarginal	69	R Supp Motor Ar
31	L Angular	70	R Rolandic Oper
32	L Precuneus	71	R Front Inf Orb
33	L Paracentr Lob	72	R Front Inf Tri
34	L Heschl	73	R Front Inf Ope
35	L Temporal Sup	74	R Front Mid Orb
36	L Tempr Pol Sup	75	R Front Mid
37	L Temporal Mid	76	R Front Sup Orb
38	L Tempr Pol Mid	77	R Frontal Sup
39	L Temporal Inf	78	R Precentral

Table SI-1. Cortical regions of the AAL areas.

BIBLIOGRAPHY

Ableidinger, M., Buckwar, E., & Hinterleitner, H. (2017). *A Stochastic Version of the Jansen and Rit Neural Mass Model: Analysis and Numerics. Journal of Mathematical Neuroscience* (Vol. 7). The Author(s). https://doi.org/10.1186/s13408-017-0046-4

Achard, S. (2006). A Resilient, Low-Frequency, Small-World Human Brain Functional Network with Highly Connected Association Cortical Hubs. *Journal of Neuroscience*, *26*(1), 63–72. https://doi.org/10.1523/JNEUROSCI.3874-05.2006

Ahmadizadeh, S., Karoly, P. J., Nešić, D., Grayden, D. B., Cook, M. J., Soudry, D., & Freestone, D. R. (2018). *Bifurcation analysis of two coupled Jansen-Rit neural mass models. PLoS ONE* (Vol. 13). https://doi.org/10.1371/journal.pone.0192842

Bansal, K., Medaglia, J. D., Bassett, D. S., Vettel, J. M., & Muldoon, S. F. (2018). Data-driven brain network models predict individual variability in behavior, 1–26. https://doi.org/arXiv:1802.08747v1

Bansal, K., Nakuci, J., & Muldoon, S. F. (2018). Personalized brain network models for assessing structure-function relationships, 1–13. Retrieved from https://arxiv.org/pdf/1802.00473.pdf

Bassett, D. S., & Sporns, O. (2017). Network neuroscience. *Nature Neuroscience*, *20*(3), 353–364. https://doi.org/10.1038/nn.4502

Breakspear, M. (2017). Dynamic models of large-scale brain activity. *Nature Neuroscience*, *20*(3), 340–352. https://doi.org/10.1038/nn.4497

Cabral, J., Hugues, E., Sporns, O., & Deco, G. (2011a). Role of local network oscillations in resting-state functional connectivity. *NeuroImage*, *57*(1), 130–139. https://doi.org/10.1016/j.neuroimage.2011.04.010

Cabral, J., Hugues, E., Sporns, O., & Deco, G. (2011b). Role of local network oscillations in resting-state functional connectivity. *NeuroImage*, *57*(1), 130–139. https://doi.org/10.1016/j.neuroimage.2011.04.010

Cabral, J., Kringelbach, M. L., & Deco, G. (2012). Functional graph alterations in schizophrenia: a result from a global anatomic decoupling? *Pharmacopsychiatry*, *45 Suppl 1*, 57–64. https://doi.org/10.1055/s-0032-1309001

Cabral, J., Luckhoo, H., Woolrich, M., Joensson, M., Mohseni, H., Baker, A., … Deco, G. (2014). Exploring mechanisms of spontaneous functional connectivity in MEG: How delayed network interactions lead to structured amplitude envelopes of band-pass filtered oscillations. *NeuroImage*, *90*, 423–435. https://doi.org/10.1016/j.neuroimage.2013.11.047

Cavaleiro Miranda, P., Mekonnen, A., Salvador, R., & Ruffini, G. (2012). The electric field in the cortex during transcranial current stimulation. *NeuroImage*, *70*.

David, O., & Friston, K. J. (2003). A neural mass model for MEG/EEG: Coupling and neuronal dynamics. *NeuroImage*, *20*(3), 1743–1755. https://doi.org/10.1016/j.neuroimage.2003.07.015

Deco, G., Jirsa, V. K., & McIntosh, A. R. (2011). Emerging concepts for the dynamical organization of resting-state activity in the brain. *Nature Reviews Neuroscience*, *12*(1), 43–56. https://doi.org/10.1038/nrn2961

Deco, G., Jirsa, V., McIntosh, A. R., Sporns, O., & Kötter, R. (2009). Key role of coupling, delay, and noise in resting brain fluctuations. *Proceedings of the National Academy of Sciences*, *106*(25), 10302–10307. https://doi.org/10.1073/pnas.0901831106

Feischl, M. (2017). Optimal adaptivity for non-symmetric FEM/BEM coupling, 1–45. Retrieved from http://arxiv.org/abs/1710.06082

Fischer, D. B., Fried, P. J., Ruffini, G., Ripolles, O., Salvador, R., Banus, J., … Fox, M. D. (2017). Multifocal tDCS targeting the resting state motor network increases cortical excitability beyond traditional tDCS targeting unilateral motor cortex. *NeuroImage*, *157*, 34–44. https://doi.org/10.1016/j.neuroimage.2017.05.060

Gong, G., Rosa-Neto, P., Carbonell, F., Chen, Z. J., He, Y., & Evans, A. C. (2009). Age- and Gender-Related Differences in the Cortical Anatomical Network. *Journal of Neuroscience*, *29*(50), 15684–15693. https://doi.org/10.1523/JNEUROSCI.2308-09.2009

Grimbert, F. and F. (2005). Analysis of Jansen's model of a single cortical column. *Writing*.

Hagmann, P., Kurant, M., Gigandet, X., Thiran, P., Wedeen, V. J., Meuli, R., & Thiran, J. P. (2007). Mapping human whole-brain structural networks with diffusion MRI. *PLoS ONE*, *2*(7). https://doi.org/10.1371/journal.pone.0000597

Hassan, M., Dufor, O., Merlet, I., Berrou, C., & Wendling, F. (2014). EEG source connectivity analysis: From dense array recordings to brain networks. *PLoS ONE*, *9*(8). https://doi.org/10.1371/journal.pone.0105041

Hipp, J. F., Hawellek, D. J., Corbetta, M., Siegel, M., & Engel, A. K. (2012). Large-scale cortical correlation structure of spontaneous oscillatory activity. *Nature Neuroscience*, *15*(6), 884–890. https://doi.org/10.1038/nn.3101

Hodgkin, A. L., & Huxley, A. F. (1990). A quantitative description of membrane current and its application to conduction and excitation in nerve. *Bulletin of Mathematical Biology*, *52*(1–2), 25–71. https://doi.org/10.1007/BF02459568

Honey, C. J., Kötter, R., Breakspear, M., & Sporns, O. (2007). Network structure of cerebral cortex shapes functional connectivity on multiple time scales. *Proceedings of the National Academy of Sciences*, *104*(24), 10240–10245. https://doi.org/10.1073/pnas.0701519104

Jansen, B. H., & Rit, V. G. (1995). Electroencephalogram and visual evoked potential generation in a mathematical model of coupled cortical columns. *Biological Cybernetics*, *73*(4), 357–366. https://doi.org/10.1007/BF00199471

Jansen, B. H., Zouridakis, G., & Brandt, M. E. (1993). A neurophysiologically-based mathematical model of flash visual evoked potentials. *Biological Cybernetics*, *68*(3), 275–283. https://doi.org/10.1007/BF00224863

Jirsa, V. K., Proix, T., Perdikis, D., Woodman, M. M., Wang, H., Bernard, C., … Chauvel, P. (2017). The Virtual Epileptic Patient: Individualized whole-brain models of epilepsy spread. *NeuroImage*, *145*, 377–388. https://doi.org/10.1016/j.neuroimage.2016.04.049

Kunze, T., Hunold, A., Haueisen, J., Jirsa, V., & Spiegler, A. (2016). Transcranial direct current stimulation changes resting state functional connectivity: A large-scale brain network modeling study. *NeuroImage*, *140*, 174–187. https://doi.org/10.1016/j.neuroimage.2016.02.015

Kurbatova, P., Wendling, F., Kaminska, A., Rosati, A., Nabbout, R., Guerrini, R., … Benquet, P. (2016). Dynamic changes of depolarizing GABA in a computational model of epileptogenic brain: Insight for Dravet syndrome. *Experimental Neurology*, *283*(Pt A), 57—72. https://doi.org/10.1016/j.expneurol.2016.05.037

Liang, Z., Duan, X., Su, C., Voss, L., Sleigh, J., & Li, X. (2015). A pharmacokinetics-neural mass model (PK-NMM) for the simulation of EEG activity during propofol anesthesia. *PLoS ONE*, *10*(12), 1–21. https://doi.org/10.1371/journal.pone.0145959

Lodato, S., & Arlotta, P. (2015). Generating Neuronal Diversity in the Mammalian Cerebral Cortex. *Annual Review of Cell and Developmental Biology*, *31*, 699–720. https://doi.org/10.1146/annurev-cellbio-100814-125353

Lopes da Silva, F. H., Hoeks, A., Smits, H., & Zetterberg, L. H. (1974). Model of brain rhythmic activity - The alpha-rhythm of the thalamus. *Kybernetik*, *15*(1), 27–37. https://doi.org/10.1007/BF00270757

Merlet, I., Birot, G., Salvador, R., Molaee-Ardekani, B., Mekonnen, A., Soria-Frish, A., … Wendling, F. (2013). From Oscillatory Transcranial Current Stimulation to Scalp EEG Changes: A Biophysical and Physiological Modeling Study. *PLoS ONE*, *8*(2), 1–12. https://doi.org/10.1371/journal.pone.0057330

Molaee-Ardekani, B., Márquez-Ruiz, J., Merlet, I., Leal-Campanario, R., Gruart, A., Sánchez-Campusano, R., … Wendling, F. (2013). Effects of transcranial Direct Current Stimulation (tDCS) on cortical activity: A computational modeling study. *Brain Stimulation*, *6*(1), 25–39. https://doi.org/10.1016/j.brs.2011.12.006

Mountcastle, V. B. (1997). The columnar organization of the neocortex. *Brain*, *120*(4), 701–722. https://doi.org/10.1093/brain/120.4.701

Mukamel, R., Gelbard, H., Arieli, A., Hasson, U., Fried, I., & Malach, R. (2005). Neuroscience: Coupling between neuronal firing, field potentials, and fMRI in human auditory cortex. *Science*, *309*(5736), 951–954. https://doi.org/10.1126/science.1110913

Muldoon, S. F., Pasqualetti, F., Gu, S., Cieslak, M., Grafton, S. T., Vettel, J. M., & Bassett, D. S. (2016). Stimulation-Based Control of Dynamic Brain Networks. *PLoS Computational Biology*, *12*(9). https://doi.org/10.1371/journal.pcbi.1005076

Ponce-Alvarez, A., Deco, G., Hagmann, P., Romani, G. L., Mantini, D., & Corbetta, M. (2015). Resting-State Temporal Synchronization Networks Emerge from Connectivity Topology and Heterogeneity. *PLoS Computational Biology*, *11*(2), 1–23. https://doi.org/10.1371/journal.pcbi.1004100

Proix, T., Spiegler, A., Schirner, M., Rothmeier, S., Ritter, P., & Jirsa, V. K. (2016). How do parcellation size and short-range connectivity affect dynamics in large-scale brain network models? *NeuroImage*, *142*, 135–149. https://doi.org/10.1016/j.neuroimage.2016.06.016

Ruffini, G. (2015). Application of the reciprocity theorem to EEG inversion and optimization of EEG-driven transcranial current stimulation (tCS, including tDCS, tACS, tRNS), *29*(2013), 1–11. Retrieved from http://arxiv.org/abs/1506.04835

Ruffini, G. (2016). *Conscious Brain-to-Brain Communication Using Noninvasive Technologies. Closed Loop Neuroscience*. Elsevier Inc. https://doi.org/10.1016/B978-0-12-802452-2.00018-4

Tzourio-Mazoyer, N., Landeau, B., Papathanassiou, D., Crivello, F., Etard, O., Delcroix, N., … Joliot, M. (2002). Automated anatomical labeling of activations in SPM using a macroscopic anatomical parcellation of the MNI MRI single-subject brain. *NeuroImage*, *15*(1), 273–289. https://doi.org/10.1006/nimg.2001.0978

van Rotterdam, A., Lopes da Silva, F. H., van den Ende, J., Viergever, M. A., & Hermans, A. J. (1982a). A model of the spatial-temporal characteristics of the alpha rhythm. *Bulletin of Mathematical Biology*, *44*(2), 283–305. https://doi.org/10.1007/BF02463252

van Rotterdam, A., Lopes da Silva, F. H., van den Ende, J., Viergever, M. A., & Hermans, A. J. (1982b). A model of the spatial-temporal characteristics of the alpha rhythm. *Bulletin of Mathematical Biology*, *44*(2), 283–305. https://doi.org/10.1007/BF02463252

Wendling, F., Bartolomei, F., Bellanger, J. J., & Chauvel, P. (2002). Epileptic fast activity can be explained by a model of impaired GABAergic dendritic inhibition. *European Journal of Neuroscience*, *15*(9), 1499–1508. https://doi.org/10.1046/j.1460-9568.2002.01985.x

Wendling, F., Bellanger, J. J., Bartolomei, F., & Chauvel, P. (2000). Relevance of nonlinear lumped-parameter models in the analysis of depth-EEG epileptic signals. *Biological Cybernetics*, *83*(4), 367–378. https://doi.org/10.1007/s004220000160

Wendling, F., Benquet, P., Bartolomei, F., Jirsa, V., Wendling, F., Benquet, P., … Jirsa, V. (2016). Computational models of epileptiform activity . To cite this version : Computational models of epileptiform activity, 233–251.

Wendling, F., & Chauvel, P. (2008). Transition to Ictal Activity in Temporal Lobe Epilepsy: Insights From Macroscopic Models. *Computational Neuroscience in Epilepsy*, 356–386. https://doi.org/10.1016/B978-012373649-9.50026-0

Wendling, F., Chauvel, P., Biraben, A., & Bartolomei, F. (2010). From Intracerebral EEG Signals to Brain Connectivity: Identification of Epileptogenic Networks in Partial Epilepsy. *Frontiers in Systems Neuroscience*, *4*(November), 1–13. https://doi.org/10.3389/fnsys.2010.00154

Wendling, F., Heilman, A. D., Quattrochi, J., Bartolomei, F., Mina, F., Huneau, C., & Benquet, P. (2012). Interictal spikes, fast ripples and seizures in partial epilepsies - combining multi-level computational models with experimental data. *European Journal of Neuroscience*, *78*(2), 2164–2177. https://doi.org/10.1111/j.1460-9568.2012.08039.x

Wendling, F., Hernandez, A., Bellanger, J.-J., Chauvel, P., & Bartolomei, F. (2005). Interictal to ictal transition in human temporal lobe epilepsy: insights from a computational model of intracerebral EEG. *Journal of Clinical Neurophysiology : Official Publication of the American Electroencephalographic Society*, *22*(5), 343–356. https://doi.org/00004691-200510000-00006 [pii]